

Quantum Estimation in Strong Fields: *in situ* ponderomotive sensing

A. S. Maxwell, A. Serafini, S. Bose, and C. Figueira de Morisson Faria

Department of Physics & Astronomy, University College London,

Gower Street, London, WC1E 6BT, United Kingdom

(Dated: October 25, 2021)

We develop a new framework to optimize and understand uncertainty from *in situ* strong field measurements of laser field parameters. We present the first derivation of quantum and classical Fisher information for an electron undergoing strong-field ionization. This is used for parameter estimation and to characterize the uncertainty of the ponderomotive energy, directly proportional to laser intensity. In particular, the quantum and classical Fisher information for the momentum basis displays quadratic scaling over time. This can be linked to above-threshold ionization interference rings for measurements in the momentum basis and to the ‘ponderomotive phase’ for the ‘ideal’ quantum measurements. Preferential scaling is found for increasing laser pulse length and intensity. We use this to demonstrate for *in situ* measurements of laser intensity, that high resolution momentum spectroscopy has the capacity to reduce the uncertainty by over 25 times compared to measurements employing the ionization rate, while using the ‘ideal’ quantum measurement would reduce it by a further factor of 2.6. A minimum uncertainty of the order $2.8 \times 10^{-3}\%$ is theorized for this framework. Finally, we examine previous *in situ* measurements formulating a measurement that matches the experimental procedure and suggest how to improve this.

I. INTRODUCTION

The time-averaged quiver energy of an electron in an external laser field, known as the ponderomotive energy U_p , is a key concept in strong-field laser-matter interaction (intensities in the range $10^{13} - 10^{20}$ W/cm²). For instance, cutoff laws for phenomena such as above-threshold ionization (ATI) [1–3] and high-order harmonic generation (HHG) [4], and momentum constraints in nonsequential double and multiple ionization (NSDI, NSMI) [5–7] are universal functions of U_p . This stems from the physical mechanism behind them, namely the laser-induced recollision or recombination of an electron with its parent ion [8, 9]. The active electron is freed close to the peak of the field, propagates in the continuum and it is driven back to the target near a field crossing. The kinetic energy acquired in the continuum then is released upon a non-linear interaction with the target, either as high-energy photon or photoelectron. Because a typical field cycle is roughly a few femtoseconds, these processes occur within hundreds of attoseconds (10^{-18} s).

An attosecond is roughly the time it takes for an electron to travel through atomic distances. Thus, strong-field phenomena allow an unprecedented control over real-time electron dynamics [10–12]. They provide tools for dealing with fundamental questions such as tunneling times [13–15], or electron migration in small [16, 17] and larger molecules [18–21], and may pave the way for optoelectronic computers up to 10,000 times faster than existing devices [22, 23]. Applications such as ultrafast photoelectron holography [24, 25] or high-harmonic spectroscopy [26] are also quite sensitive to the target and the field.

Unfortunately, many of the laser field parameters cannot be accurately measured. This is particularly true for the laser intensity, where it is common for experiments to cite 10 – 20% uncertainty. The ponderomotive energy

is directly proportional to and usually determined by the laser intensity. This lack of precision hinders progress, as the system’s dynamics vary critically with U_p . A well-known example is the boundary between the multiphoton and tunneling regimes, determined by the Keldysh parameter $\gamma = \sqrt{I_p/(2U_p)}$, where I_p denotes the ionization potential, which indicates the electron’s prevalent ionization mechanism (for a review see [27]). Other critical scenarios involve resonances with ponderomotively upshifted bound states [28–34], or giant resonances in multielectron systems [35–38]. The intensity also determines the below-threshold regime in NSDI [7], for which excitation and quantum interference become important [39–41]. Thus, it must be accurately known.

In situ measurements are ideally suited to attoscience, as they exploit the high sensitivity and nonlinearity of strong-field phenomena with regard to the laser field intensity. While early work focused on the yields of singly and doubly charged ions [42, 43], the photoelectron momentum distributions obtained from time of flight spectrometers, velocity map imaging or cold target recoil ion momentum spectroscopy (COLTRIMS) enabled momentum-based *in situ* measurements. This made it possible to determine the driving-field intensity [44] by mapping it to the final electron momentum via a classical equation of motion [45]. Including a quasi-static ionization rate and the temporal and spatial variation of the laser beam improved the accuracy and led to fitting errors of 10% [46] and 4% [47], respectively. However, due to uncertainty in other experimental parameters an overall accuracy of 8% was reported in [47]. Important breakthroughs have been achieved for photoelectron spectra from atomic hydrogen in a few-cycle linearly polarized pulse, which were fitted to those computed with the time-dependent Schrödinger equation (TDSE) [48–50]. This resulted in uncertainties of 1% in the intensity [48], and of 2% in the carrier-envelope phase [50]. Recently, the first

in situ measurement of ellipticity was performed with an uncertainty of 0.7% for xenon in a nearly circularly polarized field using ratios of intensity measurements [51]. This was achieved by separately measuring the intensity of the two linear field components and taking the ratio.

Despite this progress, the majority of strong field experiments still report laser intensity uncertainties of around 10%. *In situ* measurements can do better but the methods vary considerably depending on the experimental setup [49]. They often require ad-hoc relations or fitting processes, which (as black box approaches) give limited understanding of the mechanisms behind the laser intensity uncertainty. No general framework has been applied to date to identify and understand the main processes that affect such uncertainties and sensitivities in attoscience. Yet, such a framework does exist, and is provided by the methods of quantum metrology [52–54], which offer tools to evaluate and possibly improve the uncertainties. In mathematical terms, such methods are based on the evaluation of quantum and classical Fisher informations [55, 56], yielding proportionality factors for the scaling of the uncertainty on a parameters estimation. Such methods have been applied to practical cases with great success, especially for optical fields in the quantum regime, leading to enhanced optical-phase tracking [57, 58] and, notably, to the super-resolution of incoherent light sources [59–64]

Put simply, the classical Fisher information gives the uncertainty per measurement for a particular measurement set-up, while the quantum Fisher information yields the minimal possible uncertainty for any conceivable positive-operator valued measurement (POVM). These quantities can elucidate trends and physical mechanisms affecting the achieved uncertainty and may point to ways to reduce its value. It is important to emphasize that estimation schemes inspired by the evaluation of quantum and classical Fisher informations harness fully coherent quantum effects, and require full knowledge of the quantum state. Notably, quantum entanglement among distinct probes is well-known to improve the uncertainty scaling [52] but, less ambitiously, even coherence related to single-probe interference effects can be exploited to this aim. This is precisely what we set out to show in this study, by analysing the full quantum state within the validity range of the strong field approximation.

Quantum interference has *indeed* proved a vital and integral part of strong field and attosecond physics. Laser-induced ionization and/or recollision occurs at specific times within a laser cycle, which leads to well-defined phase shifts with regard to the field. Seminal examples are the high-order harmonic phase, which is critical for HHG propagation and attosecond-pulse generation [65] and the inter-cycle interference rings that form in ATI photoelectron momentum distribution [2, 66]. Furthermore, recollision at spatially separated centres leads to interference patterns that encode structural features in molecules [10, 67], and, recently, quantum interference has been reported in NSDI [39–41]. A key question

within attosecond imaging of matter is how to retrieve quantum phase differences from photoelectron or high-harmonic spectra. Examples of interferometric schemes are the Reconstruction of Attosecond Burst By Interferences of Two-photons Transitions (RABBIT) technique [68], the attosecond streak camera [69], the Spectral Phase Interferometry for the Direct Electric Field Reconstruction (SPIDER) [70] and the Frequency Resolved Optical Gating (FROG) [71] (for a review see [72]), and time-resolved photoelectron holography, which uses phase differences between different electron pathways to extract information about the target [24, 73]. The strongest and most robust interference effects tend to be those directly related to the strong field laser field. One primary example of such a quantum interference effect being ATI peaks/ rings. These are strongly dependent on the driving-field intensity [66] and can be used for intensity calibration. By computing the Fisher information using a quantum-orbit model we may turn this interference on or off and thus thoroughly investigate the effect on uncertainty in laser intensity measurements.

In this article we will use the well-known workhorse of attoscience, the strong field approximation (SFA), see [74] for a review, as the underlying model with which to compute the quantum and classical Fisher information. To our knowledge the quantum and classical Fisher information have not been computed in the context of strong-field ionization before. As such, in this first study, we will focus on the broader trends of the uncertainty due to the laser field rather than differences in targets. The SFA is approximate and neglects the effect of the binding potential on the photoelectrons. The simplicity of the SFA allows for analytical trends to be extracted and for a faster and easier construction of the Fisher information. The computation of the Fisher information requires the evaluation of high-oscillatory integrals, which leads to computing of the order of a million transition amplitudes per value calculated. Thus, it is not clear that it would be possible to use the numerical solutions of the TDSE for this purpose.

The structure of this article is as follows: In Sec. II the relevant theory for the SFA for a zero range potential is introduced (Sec. II A) and the quantum and classical Fisher information along with their relation to the uncertainty are defined (Sec. II C). Next in Sec. III the procedure for computing the quantum and classical Fisher information with the SFA (and similar orbit based models) is outlined. Additionally, using this definition some general trends are identified analytically. Following these analytical results in Sec. IV we present numerical calculations of the Fisher information. In Sec. IV A we continue to explore the general trends and establish a strong link to interference, while in Sec. IV B we examine previous *in situ* experiments to measure the laser intensity. Using the classical and quantum Fisher information we predict the minimum possible uncertainty and make suggestions on how the measurement could be improved by change experimental set-up field parameters and the measurement

basis. Finally, in Sec. V we sum up our findings, discuss their implication in the context of the recent strong field results and what the next step is with this framework.

II. BACKGROUND

A. Strong field approximation

Throughout, we consider an electron in a strong laser field and a zero range potential, whose Hamiltonian (under the dipole approximation) reads

$$\hat{H}(t) = \frac{1}{2}\hat{\mathbf{p}}^2 + H_I(t) + \hat{V} \quad (1)$$

and the zero range (regularized) potential is given by

$$\hat{V} = -\frac{2\pi}{\sqrt{I_p}}\delta(\mathbf{r})\frac{\partial}{\partial r}r. \quad (2)$$

The zero-range potential is advantageous for the implementation of the SFA, as it supports a single bound state and plane waves are a good approximation for the continuum; see [75] for more details. We employ atomic units throughout (denoted a.u.), where the elementary charge, electron mass and \hbar are set to one, $e = m = \hbar = 1$. The laser interaction Hamiltonian reads as $H_I(t) = 2\hat{\mathbf{p}} \cdot \mathbf{A}(t) + \mathbf{A}(t)^2$ in the velocity gauge and $H_I(t) = -\hat{\mathbf{r}} \cdot \mathbf{E}(t)$ in the length gauge. The atomic Hamiltonian $H_0 = \frac{1}{2}\hat{\mathbf{p}}^2 + \hat{V}$, describes the electron in the bound and scattering states. The Volkov Hamiltonian $H_V = \frac{1}{2}\hat{\mathbf{p}}^2 + H_I(t)$ describes a free electron propagating in a laser field [76, 77].

The electron starts in the only bound state of the zero range potential $|\psi(t=0)\rangle = |0\rangle$, with

$$\langle r|0\rangle = \frac{(I_p)^{1/4} \exp(-\sqrt{I_p}r)}{2\pi r}. \quad (3)$$

The full time evolution operator $U(t,0)$ can be written as

$$U(t,0) = U_0(t,0) - i \int_0^t dt' U(t,t') \hat{H}_I(t') U_0(t',0). \quad (4)$$

The time evolution operators $U_0(t,t')$, $U_V(t,t')$ and $U(t,t')$ describe propagation for the atomic, Volkov and full Hamiltonians, respectively. In the strong field the full time-evolution operator in the integrand in Eq. (4) can be replaced by the Volkov time-evolution operator, which amounts to neglecting the potential for the ionised electron. The state of our system with this approximation can then be written as

$$|\psi(t)\rangle = U_0(t,0)|0\rangle - i \int_0^t dt' U_V(t,t') \hat{H}_I(t') U_0(t',0)|0\rangle. \quad (5)$$

We write Eq. (5) in the velocity gauge but apply a unitary transformation to the laser interaction Hamiltonian

to convert to the length gauge. It is possible in Eq. (5) to replace the interaction Hamiltonian with the potential, which ultimately will make the computations simpler [78]. The Volkov time-evolution operator can be written as

$$U_V(t,t') = \int d^3\mathbf{p} |\psi_V^{\mathbf{p}}(t)\rangle \langle \psi_V^{\mathbf{p}}(t')|, \quad (6)$$

where $|\psi_V^{\mathbf{p}}(t)\rangle = |\mathbf{p} + \mathbf{A}(t)\rangle e^{-iA_V(\mathbf{p},t)}$ and $A_V(\mathbf{p},t) = \frac{1}{2} \int dt (\mathbf{p} + \mathbf{A}(t))^2$. The atomic time-evolution operator is given by $U_0(t',0) = \exp(iI_p t')$. Substituting Eq. (6) and the atomic time evolution operator into Eq. (5) gives

$$|\psi(t)\rangle = \exp(iI_p t)|0\rangle - i \int_0^t dt' \int d^3\mathbf{p} \times e^{iA_V(\mathbf{p},t)} |\mathbf{p} + \mathbf{A}(t)\rangle \langle \mathbf{p} + \mathbf{A}(t')| e^{-iA_V(\mathbf{p},t')} \hat{V} e^{iI_p t'} |0\rangle, \quad (7)$$

which, with a phase transformation can be written compactly as

$$|\psi(t)\rangle = |0\rangle - i \int d^3\mathbf{p} e^{-iS(\mathbf{p},t)} |\tilde{\mathbf{p}}(t)\rangle M(\mathbf{p}), \quad (8)$$

where $\tilde{\mathbf{p}}(t) = \mathbf{p} + \mathbf{A}(t)$ and

$$M(\mathbf{p}) := \int dt' d(\mathbf{p},t') e^{iS(\mathbf{p},t')}, \quad (9)$$

with $d(\mathbf{p},t') = \langle \mathbf{p} + \mathbf{A}(t') | \hat{V} | 0 \rangle$ and $S(\mathbf{p},t) = I_p t + \frac{1}{2} \int dt (\mathbf{p} + \mathbf{A}(t))^2$.

In order to calculate the integral over t' we employ the saddle-point approximation and compute stationary action for t' [28], which gives

$$\delta_{t'} S(\mathbf{p},t') = 0 \implies (\mathbf{p} + \mathbf{A}(t'))^2 = -2I_p. \quad (10)$$

We use

$$\mathbf{A}(t) = 2\sqrt{U_p} F(t) \cos(\omega t + \phi) \hat{e}_{\parallel},$$

where ϕ is the carrier envelope phase and the pulse envelope $F(t) = e^{-2\ln(2)\frac{t^2}{\tau^2}}$ for a Gaussian pulse with a pulse length τ . For a monochromatic field $F(t) = 1$ and $\phi = 0$. Here, \hat{e}_{\parallel} is the unit vector in the polarization direction of the linear field, often associated with the z -axis. The ponderomotive energy is given by

$$U_p = \frac{I}{2c\epsilon_0\omega^2}, \quad (11)$$

where c and ϵ_0 are the speed of light and vacuum permittivity, given by $c \approx 137.036$ and $\epsilon_0 = 1/(4\pi)$ in atomic units. For a monochromatic field Eq. (10) is analytically invertible to give the periodic solutions

$$t'_{en} = \frac{2\pi(n-e)}{\omega} - \frac{(-1)^e}{\omega} \arccos\left(\frac{-p_{\parallel} + (-1)^e i\sqrt{2I_p + p_{\perp}}}{2\sqrt{U_p}}\right), \quad (12)$$

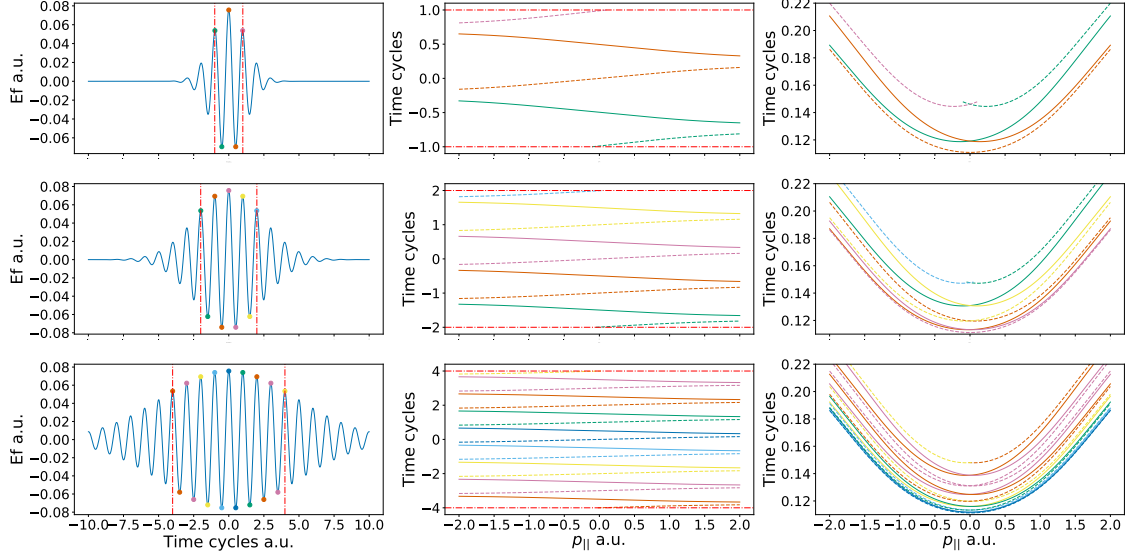


FIG. 1. Solutions of the saddle point Eq. (10) for 3 Gaussian pulse of 2, 4 and 8 cycles [top, middle and bottom rows]. Left column: the real part of the time of ionization on the electric field for a near zero momentum. Middle column: real parts of ionization times for varying p_{\parallel} momentum. Right column: The imaginary part of ionization times for varying p_{\parallel} momentum. Dotted lines are drawn vertically to denote the full-width half-maximum of each field. The peak intensity and wavelength of all fields shown is 2×10^{14} W/cm² [$U_p = 0.44$ a.u.] and $\lambda = 800$ nm [$\omega = 0.057$ a.u.], respectively. An ionization potential $I_p = 0.5$ a.u. is used for the zero range potential. The CEPs are all $\phi = \pi/2$, to make the pulses symmetric. The coloured dots mark the real part of solutions of the ionization Eq. (10) on the laser field for a final momentum of $(p_{\parallel}, p_{\perp}) = (0.002, 0.1)$ a.u. The times of ionization in the middle and right column are plotted using $p_{\perp} = 0.1$ a.u., where p_{\perp} is the momentum co-ordinate perpendicular to the laser field polarisation. Note the colour used for the dots on the laser field corresponds the colour used for the real and imaginary plots of the solutions in the middle and right columns.

where $e = 0, 1$ denotes pairs of intracycle solutions within the same field cycle and $n = 1, 2, \dots$ denotes intercycle periodic solutions in each laser cycle. In the case of a laser pulse Eq. (10) must be solved numerically, but the solutions have the same form of intracycle and intercycle solutions.

Using the saddle point approximation the transition amplitude can be written as

$$M(\mathbf{p}) = \sum_{n=0}^{N_c-1} \sum_{e=0}^1 \sqrt{\frac{2\pi i}{\partial^2 S(\mathbf{p}, t'_{en}) / \partial t'^2}} \langle \mathbf{p} + \mathbf{A}(t') | \hat{V} | 0 \rangle e^{iS(\mathbf{p}, t'_{en})}. \quad (13)$$

For the monochromatic case this can be rewritten as

$$|M(\mathbf{p})|^2 = \left| \sum_{e=0}^1 \sqrt{\frac{2\pi i}{\partial^2 S(\mathbf{p}, t'_{e0}) / \partial t'^2}} \langle \mathbf{p} + \mathbf{A}(t') | \hat{V} | 0 \rangle e^{iS(\mathbf{p}, t'_{e0})} \right|^2, \quad (14)$$

where

$$\Omega(\mathbf{p}) = \frac{\cos \left[\frac{2\pi N_c}{\omega} \left(U_p + I_p + \frac{1}{2} |\mathbf{p}|^2 \right) \right] - 1}{\cos \left[\frac{2\pi}{\omega} \left(U_p + I_p + \frac{1}{2} |\mathbf{p}|^2 \right) \right] - 1}. \quad (15)$$

Eq. (14) states that intracycle and intercycle interference are separable for monochromatic fields. Explicitly, intercycle interference is given by Eq. (15), which gives a quantization condition for rings of constant energy in the momentum space.

Note the SFA model presented here is cylindrically symmetric. Thus, it may be full parametrized by the final momentum coordinates p_{\parallel} and p_{\perp} , parallel and perpendicular to the laser field polarization, respectively.

B. Features of the Model

Before deriving the quantum and classical Fisher information, we first briefly present the possible ionization times that the electron may take via the quantum orbit model for different pulse lengths, and how this affects the momentum dependent transitions amplitude.

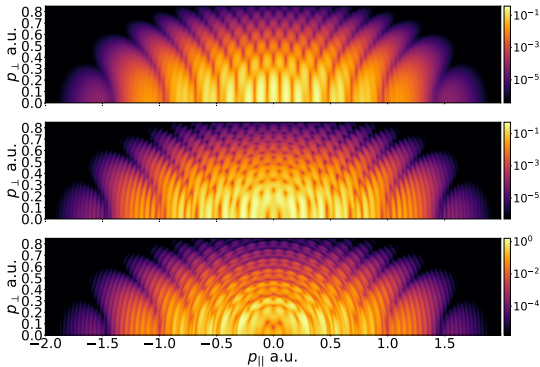


FIG. 2. Momentum dependent transition amplitude computed for the same target and field parameters as Fig. 1, which corresponds to 2, 4 and 8 cycle Gaussian pulses from top to bottom. Further examples of such distributions can be found in [79].

In Fig. 1 and Fig. 2 the solutions of Eq. (10) and transition amplitude show a few well-known physical properties of the system:

- i The real part of the times of ionization occur at the electric field maxima for $p_{\parallel} = 0$ [Fig. 1 left column].
- ii Away from $p_{\parallel} = 0$ the solutions move slowly towards the field crossings [Fig. 1 middle column].
- iii The imaginary part gives a good indication of the photoelectron yield, with a lower value giving a higher yield [Fig. 1 right column].
- iv The orbits occurring nearest to the electric field maximum have the highest yield.
- v The overall yield is maximum at $\mathbf{p} = 0$ [Fig. 2].
- vi The shorter laser pulses display characteristic finger-like fringes, due to interference between orbits occurring within a single laser cycle.
- vii The long pulse also demonstrate interference rings between laser cycles, known as above-threshold ionization (ATI) rings.

C. The Fisher Information

A quantum measurement described by a positive-operator valued measure (POVM) $K_{\mu} : \sum_{\mu} K_{\mu}^{\dagger} K_{\mu} = \mathbf{1}$ allows for the estimation of an unknown parameter g , encoded in a quantum state ϱ_g , with an uncertainty limited by the classical Cramér-Rao bound [55, 56]:

$$\Delta g \geq \frac{1}{\sqrt{NI_F}}, \quad (16)$$

where N is the number of individual measurements performed and I_F is the classical Fisher information, given by

$$I_F = \sum_{\mu} \frac{(\mathcal{P}'(\mu|g))^2}{\mathcal{P}(\mu|g)} \quad (17)$$

in terms of the conditional probability $\mathcal{P}(\mu|g) = \text{Tr}[K_{\mu}^{\dagger} K_{\mu} \varrho_g]$ (while a prime ' denotes derivation with respect to the parameter g). In turn, the classical Fisher information is bounded from above by the quantum Fisher information $Q_F = \sup_{K_{\mu}} I_F$, which may be evaluated as

$$Q_F(t) = 4 \left[\langle \partial_g \psi(t) | \partial_g \psi(t) \rangle - |\langle \psi(t) | \partial_g \psi(t) \rangle|^2 \right], \quad (18)$$

where ∂_g is the derivative with respect to the measurement variable, which in our case is the ponderomotive energy U_p .

III. ANALYTICAL RESULTS

In order to compute both the classical and quantum Fisher information we must calculate the derivative of the wave function with respect to the measurement variable.

$$\partial_g |\psi(t)\rangle = -i \int d\mathbf{p} |\tilde{\mathbf{p}}(t)\rangle e^{-iS(\mathbf{p},t)} M_g(\mathbf{p},t), \quad (19)$$

where

$$M_g(\mathbf{p},t) = \int dt' f(\mathbf{p},t,t') e^{iS(\mathbf{p},t')}, \quad (20)$$

$$f(\mathbf{p},t,t') = \frac{\partial d(\mathbf{p},t')}{\partial g} + i d(\mathbf{p},t') \left(\frac{\partial S(\mathbf{p},t')}{\partial g} - \frac{\partial S(\mathbf{p},t)}{\partial g} \right). \quad (21)$$

The definition of $d(\mathbf{p},t')$ is given in Eq. (9). We are assuming that we are choosing t such that $\mathbf{A}(t) = 0$ and $|\tilde{\mathbf{p}}(t)\rangle = |\mathbf{p}\rangle$. This is achieved when laser the pulse is over or the field is maximum (hence the vector potential is at a crossing point). The transition amplitude derivative $M_g(\mathbf{p},t)$ can be computed using the same saddle points as $M(\mathbf{p})$ but just using the alternative prefactor $f(\mathbf{p},t,t')$, which saves on computational time.

A. Quantum Fisher Information

Inserting the above definitions for the wavefunction and its derivative in to Eq. (18) gives an expression for the quantum Fisher information in terms of the transitions amplitude and its 'derivative', namely

$$Q_F(t) = 4 \left\{ \int d^3\mathbf{p} |M_g(\mathbf{p},t)|^2 - \left| \int d^3\mathbf{p} \overline{M(\mathbf{p})} M_g(\mathbf{p},t) \right|^2 \right\}. \quad (22)$$

There is only one quantum Fisher information as it corresponds to the supremum of the set of classical Fisher informations over all possible POVMs, thus represent the best possible measurement and is basis independent.

B. Classical Fisher Information

In all cases the POVMs corresponding to particular experimental measurements will be on the Hilbert space $L^2(\mathbb{R}^3) \oplus \{|0\rangle\langle 0|\}$ of square integral functions on 3D space, which corresponds to measurements of the momentum (or space) on the ionized portion of the wavefunction plus the zero projector corresponding to the bound portion of the wavefunction. We will use the notation that $K_0 = |0\rangle\langle 0|$ throughout. Next, we consider various cases of measurement:

1. An idealized, infinitely precise, momentum measurement, in which the outcomes correspond exactly to the elements in the full momentum space $\mathbf{p} \in \mathbb{R}^3$. We will denote these measurements as *full* for short.
2. Coarse momentum measurement, with a tunable precision. The possible outcomes will divide momentum space into a finite number of regions. This provides a more realistic experimental measurement. We will denote these measurements as *coarse*.
3. A measurement relating to ionization yield, which will only have two outcomes. The whole momentum region will be taken as a single outcome that relates to the electron being ionized, while the bound state will relate to the other outcome and represents the electron remaining bound. These measurements will be labelled as *yield*.
4. We will also consider *spectral* measurements, where the energy of the photoelectron is measured but no angular information is collected. This will have a version with infinite precision and a coarse version, that correspond to an infinite and finite set of energy outcomes, respectively. We will refer to the full and coarse spectral measurements as *spec1* and *spec2*, respectively.

1. Full Measurements

For the momentum case we will be measuring with the POVM

$$\mathbb{1} := K_0^{full} + \int d^3\mathbf{p} K_{\mathbf{p}}^{full}, \quad (23)$$

where $K_{\mathbf{p}}^{full} = |\mathbf{p}\rangle\langle \mathbf{p}|$. Recall, the additional bound state projector simply represents the portion of the wavefunction that remains bound, however, this projector is zero when the derivative is taken in the classical Fisher information and thus it does not affect the final result but in other formulations it could play a role. The classical

Fisher information takes the form

$$I_F^{full}(t) = \int d^3\tilde{\mathbf{p}}(t) \frac{(\partial_g |-ie^{-iS(\mathbf{p},t)} M(\mathbf{p})|^2)^2}{|-ie^{-iS(\mathbf{p},t)} M(\mathbf{p})|^2} \quad (24)$$

$$I_F^{full}(t) = \int d^3\tilde{\mathbf{p}}(t) \frac{(\partial_g |M(\mathbf{p})|^2)^2}{|M(\mathbf{p})|^2}. \quad (25)$$

From the above expression it is clear for the momentum basis there is no explicit time-dependence in the classical Fisher information. The expression can further simplify to

$$I_F^{full}(t) = \int d^3\mathbf{p} \frac{4\text{Re}[M_g(\mathbf{p}, t)\overline{M(\mathbf{p})}]^2}{|M(\mathbf{p})|^2}. \quad (26)$$

Note if we remove the time dependence on the integration measure it acts to shift the centre of the integrand but the integration region is infinite. Thus, this does not affect the final result. When we compute this classical Fisher information we will refer to it as the **full** classical Fisher information.

2. Coarse Measurements

The POVM given by Eq. (23) represents momentum measurements with infinite precision. In experiment there is some uncertainty associated with the measurements. One way to represent this is with coarse measurement, where we imagine there is a discrete number of momentum bins. They can be described by the following POVM:

$$\mathbb{1} := \sum_{i=0}^N K_i^{coarse}, \quad (27)$$

where K_i^{coarse} are the projective measurements for each outcome, there are N momentum outcomes/ bins and $K_0^{coarse} = |0\rangle\langle 0|$ and corresponds to portion of the wavefunction that has not been ionized. The remaining measurement outcomes are described by

$$K_i^{coarse} = \int_{\mathcal{R}_i} d^3\mathbf{p} |\mathbf{p}\rangle\langle \mathbf{p}|. \quad (28)$$

In this equation $\mathcal{R}_i \subseteq \mathbb{R}^3$ corresponds to a region or bin in momentum space that relates to a single measurement outcome of the detector. Note $\mathcal{R}_i \cap \mathcal{R}_j = \emptyset$ if $i \neq j$ and $\bigcup_{i=1}^N \mathcal{R}_i = \mathbb{R}^3$. Inserting this in to Eq. (17) leads to

$$I_F^{coarse}(t) = \sum_{i=1}^N \frac{4\text{Re}[\int_{\mathcal{R}_i} d^3\mathbf{p} \overline{M(\mathbf{p})} M_g(\mathbf{p}, t)]^2}{\int_{\mathcal{R}_i} d^3\mathbf{p} |M(\mathbf{p})|^2}. \quad (29)$$

This form of the classical Fisher information we will refer to as the **coarse** classical Fisher information.

3. Yield Measurements

The limiting case of coarse measurement is when there is only a single region for the momentum $\mathcal{R}_1 = \mathbb{R}^3$. In this case there are only two measurement outcomes, labelled 0 and 1, which correspond to if the electron is bound or ionized, respectively, given by the following POVM

$$\mathbb{1} := K_0^{yield} + K_1^{yield}, \quad (30)$$

where

$$K_1^{yield} = \int_{\mathbb{R}^3} d^3\mathbf{p} |\mathbf{p}\rangle \langle \mathbf{p}|. \quad (31)$$

This leads to

$$I_F^{yield}(t) = \frac{4\text{Re} \left[\int d^3\mathbf{p} \overline{M(\mathbf{p})} M_g(\mathbf{p}, t) \right]^2}{\int d^3\mathbf{p} |M(\mathbf{p})|^2} \quad (32)$$

for the classical Fisher information. When we use this classical Fisher information we will refer to it as the **yield** classical Fisher information.

4. Spectral Measurements

The spectral measurement using an infinite number of energy bins is given by

$$I_F^{spec1}(t) = \int dE \frac{\mathcal{P}'(E|g)^2}{\mathcal{P}(E|g)}, \quad (33)$$

while the formula for a coarse measurement with a finite number of energy bins is given by

$$I_F^{spec2}(t) = \sum_{i=1}^N \frac{\left[\int_{E_{i-1}}^{E_i} dE \mathcal{P}'(E|g) \right]^2}{\int_{E_{i-1}}^{E_i} dE \mathcal{P}(E|g)}. \quad (34)$$

We will refer to these as the full spectra and coarse spectral classical Fisher informations, respectively. In both of these formulae $\mathcal{P}(E|g)$ is given by

$$\mathcal{P}(E|g) = \int d\Omega |M(E, \theta, \phi)|^2, \quad (35)$$

where $M(\mathbf{p})$ has been re-parametrized in terms of the energy and angular dependences and is integrated over the angles.

C. Analytical trends

1. Ponderomotive phase Q_F

In this section we argue that our measurement variable, the laser intensity, is primarily encoded via a phase difference (the ponderomotive phase) between the continuum bound part of the wave function. It is important

to note that if the photoelectron was prepared into a single continuum state with a phase that depended on the laser field intensity this would not be a physical observable and the quantum Fisher information would be zero. However, the ionization process leads to a superposition/ distribution across many continuum states and the bound state, each with their own momentum dependent phases and normalizations. This superposition of final states with different normalizations and phases (relative to the bound state) encoding the laser intensity leads to a large quantum Fisher information, and we show here it is quadratically dependent on the time exposed to the laser field.

Using Eq. (22) we can extract an approximate expression for the time dependence of the Fisher information. The transition amplitude $M(\mathbf{p})$ is independent of the final time t after the laser pulse is over due to the momentum conservation. It is only $M_g(\mathbf{p}, t)$ that is dependent on final time via the prefactor term $f(\mathbf{p}, t, t')$. We can compute the derivative

$$\frac{\partial S(\mathbf{p}, t)}{\partial U_p} = -\frac{1}{2U_p} \left[\mathbf{p} \cdot \int \mathbf{A}(t) dt + \int \mathbf{A}(t)^2 dt \right] \quad (36)$$

of the action in this prefactor, which is the part dependent on the final time. For large enough time t the $\mathbf{A}(t)^2$ integral in the prefactor will strongly dominate. Thus, the large time behaviour of the Fisher information can be derived as

$$f(\mathbf{p}, t, t') \rightarrow i \frac{d(\mathbf{p}, t')}{2U_p} \int \mathbf{A}(t)^2 dt \quad (37)$$

$$M_g(\mathbf{p}, t) \rightarrow i \int \mathbf{A}(t)^2 \frac{M(\mathbf{p})}{2U_p} \quad (38)$$

$$Q_F(t) \rightarrow \alpha \left(\frac{1}{U_p} \int \mathbf{A}(t)^2 dt \right)^2, \quad (39)$$

where

$$\alpha = \int d^3\mathbf{p} |M(\mathbf{p})|^2 \left(1 - \int d^3\mathbf{p} |M(\mathbf{p})|^2 \right). \quad (40)$$

For a monochromatic field

$$Q_F(t) \approx \alpha \left(2t + \frac{\sin(2\omega t)}{\omega U_p} \right)^2, \quad (41)$$

which means there will be quadratic scaling in the uncertainty. In the case of a Gaussian pulse

$$Q_F(t) \approx \alpha \left(\sqrt{\frac{\pi}{4 \ln(2)}} \tau \right)^2 \left(\text{erf} \left(\frac{t \sqrt{4 \ln(2)}}{\tau} \right) + e^{-\frac{\tau^2 \omega^2}{4 \ln(2)}} f_{osc}(t) \right)^2, \quad (42)$$

where

$$f_{osc}(t) = e^{i2\phi} \text{erf} \left(\frac{4 \ln(4)t - i\tau^2 \omega}{2\tau \sqrt{\ln(2)}} \right) + \text{c.c.} \quad (43)$$

and τ is the pulse length. Here $f_{osc}(t)$ is oscillatory and heavily damped by the exponential prefactor. The pulse length puts a limit on the quantum Fisher information. For $t \rightarrow \infty$ this expression becomes

$$Q_F(t) \propto \frac{\tau^2 \pi \alpha}{8 \ln(2)} \left(1 + \cos(\phi) e^{\frac{-\tau^2 \omega^2}{2 \ln(2)}} \right)^2 \quad (44)$$

It is clear that the quantum Fisher information is quadratically dependent on the laser pulse length rather than final time. For continuous wave/ monochromatic fields the final time and pulse length are the same. This quadratic dependence on the integral of the vector potential enables highly sensitive measurements of the laser intensity. We will call the A^2 phase difference between the bound and continuum parts of the wave function the ponderomotive phase, as it derives from the electron dynamics in the continuum for a free electron. In order to measure this phase directly one would need to find a basis in which the bound and final states can interfere. In practical terms, this can be achieved by considering the two pathways, where the electron ionization occurs at two separate times. While one path is ionized and the other is bound a phase difference, via the ponderomotive phase, will be acquired. This naturally occurs in strong field phenomena where at various times a portion of the electron wavefunction may ionize. The ionized portion will pick up the ponderomotive phase, while the bound portion does not. Thus, the interference of two electron pathways released at different times, such as in ATI rings, can reveal the ponderomotive phase.

2. ATI rings and classical Fisher information

In contrast to the quantum Fisher information the classical Fisher information is dependent on the measurement basis. Furthermore, if performing momentum measurements the wave function's superposition over the bound and continuum states will not reveal the ponderomotive phase. It requires the interference of more than one electron path with different phases that end in the same continuum state. In this section we will examine how interference affects the classical Fisher information. The interference of an electron ionized at two different times of equivalent laser intensity $|\mathbf{E}(t_1)| = |\mathbf{E}(t_2)|$ gives the following probability

$$\begin{aligned} |M(\mathbf{p})|^2 &= |M_1(\mathbf{p}) + M_2(\mathbf{p})|^2 \\ &= |M_1(\mathbf{p})|^2 |1 + e^{i\Delta S(\mathbf{p}, t_2, t_1)}|^2. \end{aligned} \quad (45)$$

In order to compute the classical Fisher information one needs to take the derivative

$$\begin{aligned} \partial_{U_p} (|M(\mathbf{p})|^2) &= |1 + e^{i\Delta S(\mathbf{p}, t_2, t_1)}|^2 \partial_{U_p} (|M_1(\mathbf{p})|^2) \\ &\quad - 2 \sin(\Delta S(\mathbf{p}, t_2, t_1)) \frac{\partial \Delta S(\mathbf{p}, t_2, t_1)}{\partial U_p} |M_1(\mathbf{p})|^2, \end{aligned} \quad (46)$$

with regard to the measurement variable U_p , where

$$\frac{\partial \Delta S(\mathbf{p}, t_2, t_1)}{\partial U_p} = -\frac{1}{2U_p} \left[\mathbf{p} \cdot \int_{t_1}^{t_2} \mathbf{A}(t) dt + \int_{t_1}^{t_2} \mathbf{A}(t)^2 dt \right] \quad (47)$$

The same dependence on the ponderomotive phase is apparent. The phase grows with a larger difference between ionization times, which means longer pulses will allow a larger difference in times thus increasing the momentum measurement classical Fisher information via interference. For a monochromatic field we can explicitly examine the dependence on the pulse length. The transition amplitude can be written as

$$|M_N(\mathbf{p})|^2 = \Omega_N(\mathbf{p}) |M_0(\mathbf{p})|^2, \quad (48)$$

where $M_N(\mathbf{p})$ is the transition amplitude and N denotes the number of laser cycles we consider ionization events for. $M_0(\mathbf{p})$ is the ionization events across a single cycle unit cell and $\Omega_N(\mathbf{p})$ is given by Eq. (15). The derivative of the previous expression used in the classical Fisher information is

$$\begin{aligned} \partial_{U_p} (|M_N(\mathbf{p})|^2) &= \partial_{U_p} (\Omega_N(\mathbf{p})) |M_0(\mathbf{p})|^2 \\ &\quad + \Omega_N(\mathbf{p}) \partial_{U_p} (|M_0(\mathbf{p})|^2). \end{aligned} \quad (49)$$

We can compute the derivative of $\Omega_N(\mathbf{p})$

$$\partial_{U_p} (\Omega_N(\mathbf{p})) = \chi_N(\mathbf{p}) \Omega_N(\mathbf{p}), \quad (50)$$

with

$$\begin{aligned} \chi_N(\mathbf{p}) &= \frac{2\pi}{\omega} \left(\cot \left(\frac{\pi}{\omega} (I_p + U_p + \frac{1}{2} \mathbf{p}^2) \right) \right. \\ &\quad \left. - N \cot \left(\frac{N\pi}{\omega} (I_p + U_p + \frac{1}{2} \mathbf{p}^2) \right) \right). \end{aligned} \quad (51)$$

The factor of N in the second term will lead to an N^2 dependence in the classical Fisher information, which mirrors the quadratic dependence on the pulse length in the quantum Fisher information.

IV. NUMERICAL RESULTS

A. General Trends

When using momentum *in situ* measurements to determine laser intensity it is expected that interference and in particular ATI-rings will take a prominent role as shown analytically in Sec. III C. Using an orbit based method we are able to turn interference on/ off at will and thus we have the ability to examine the effect this has on the quantum and classical Fisher information.

1. Yield vs Interference

Earlier measurements simply used the ionization yield to determine the laser intensity. In order to replicate

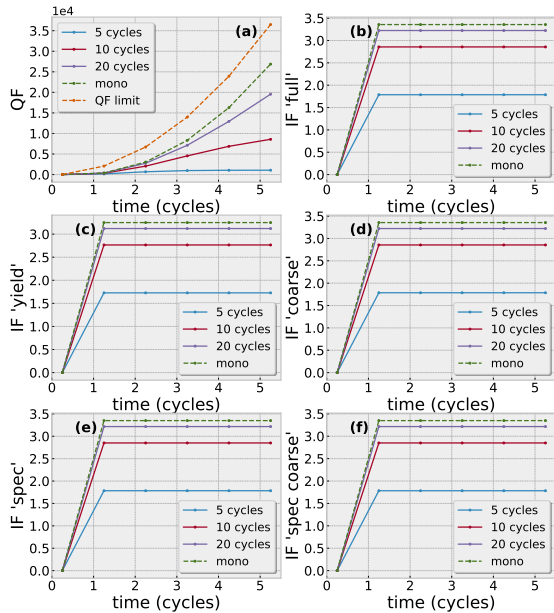


FIG. 3. The quantum (a), classical full momentum basis (b), yield basis (c), coarse basis (d), full spectral (e) and coarse spectral (f) Fisher information for a single ionisation channel. The computation has been done for three Gaussian pulses each with full-width at half maximum of 5, 10 and 20 laser cycles and a monochromatic laser for reference. The peak intensity and wavelength of all fields shown is 2×10^{14} W/cm² [$U_p = 0.44$ a.u.] and 800 nm [$\omega = 0.057$ a.u.], respectively. An ionization potential $I_p = 0.5$ a.u. is used for the zero range potential. The CEPs are all $\phi = \pi/2$, to make the pulses symmetric. The coarse momentum and spectral measurements use a resolution of 0.1 a.u. and 0.05 a.u. respectively. In the case of the coarse momentum measurement this means the regions/ bins \mathcal{R}_i from Eq. (27) are squares with sides of 0.1 a.u.

these results we start by computing the quantum and classical Fisher information using only a single ionisation channel/ orbit so that all interference effects are removed, see Fig. 3. This is a little artificial as we consider three different pulse lengths and a monochromatic field but restrict them all to a single ionisation event. This makes both the quantum and classical Fisher information smaller but allows us to probe trends without interference effects.

The quantum Fisher information is not affected by the lack of interference and as expected from Sec. III C 1. The quantum Fisher information quadratically increases with time for the monochromatic case (see Fig. 3 (a)) and for the Gaussian pulse it follows an error function, reaching a maximum at the end of the laser envelope. This is consistent with the freed electron acquiring laser intensity information for as long as it is exposed to the laser, via a

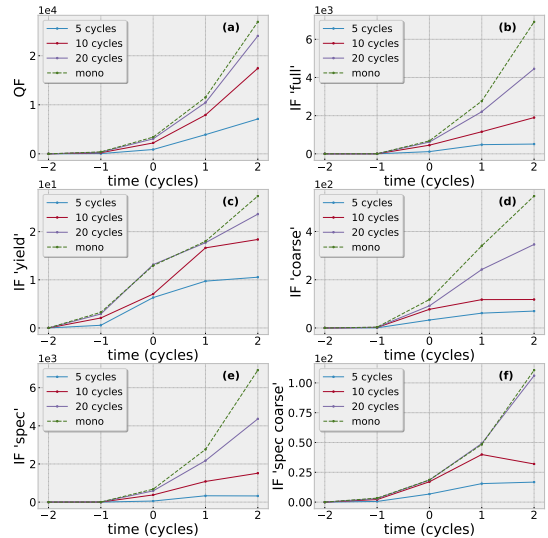


FIG. 4. The quantum and classical Fisher informations as in Fig. 3 except computed with 5 channels of ionization included to assess the effect of interference. The same field and target parameters are used as in Fig. 3.

ponderomotive phase. The quantum Fisher information effectively gives the maximum classical Fisher information for any measurement basis. Thus, measuring in some non-momentum bases the superposition of bound state with the continuum states can be exploited via interference to reveal their phases. The limit given by Eq. (41) for the quantum Fisher information is plotted on Fig. 3 and closely follows the computed value.

In contrast, the classical Fisher information increases from zero once the electron is ionized but remains constant beyond this point. Momentum measurements are blind to the ponderomotive phase if interference is neglected and give information related only to the ionization process. In addition, the canonical momentum is conserved making the transition amplitude and thus the classical Fisher information constant after ionization.

There are nearly 4 orders of magnitude difference between the classical Fisher informations and quantum Fisher information. With the interference switched off all the classical Fisher informations are equal because only the overall yield contributes to the Fisher information. So the coarse, full and spectral based measurements are all reduced to the value of the yield measurement. The yield measurement will be always a lower bound for the other measurements and thus can be used to quantify how much interference enhances other measurements. The fact that the quantum is so much larger than classical Fisher information suggests the momentum basis is not a good choice for determining laser intensity for strong field ionization if there is little or no interference.

This could have implications for very short laser pulses with full-width at half maximum of around 1 cycle. It would suggest there exists a better measurement basis built from a superposition of momentum states. In fact, it is possible that the position basis for the photoelectron would outperform the momentum basis in determining the laser intensity uncertainty for very short pulses.

In contrast, Fig. 4 includes 5 interference channels. These are all relevant channels for the 5 cycle pulse, while for the longer pulses we consider the first 5 relevant channels by order of occurrence in the pulse. This leads to large differences between the classical Fisher informations. As the time increases along the pulse, additional ionization events occur, each acting to increase the value of the various classical Fisher informations. The full classical Fisher information drastically increases quadratically with each ionization event to around 3 orders of magnitude larger than the value for a single channel. In contrast, the yield classical Fisher information does not increase very much, about 8 times the value for a single channel. However, 4 extra channels lead to more ionization yield, hence some increase in yield classical Fisher information is expected. The coarse classical Fisher information follows a behaviour roughly in-between the other two cases, increasing just over 2 orders of magnitude times the value for a single channel.

In addition, we have included the classical Fisher information, which results from making ‘spectral’ energy measurement upon the photoelectron. For longer 20-cycle and monochromatic cases this is almost identical to the full momentum measurement. Here we consider only intercycle ‘ATI’ interference, thus for long pulses the momentum dependent transition amplitude is almost spherically symmetric hence the similarity between the two. However, for shorter pulses the distributions are less symmetric and the spectral measurement performs less well. For coarse measurement with an energy resolution of 0.05 a.u. the spectral measurements are consistently 5 \times worse than the coarse momentum measurements with a resolution of 0.1 a.u. Note this level of momentum resolution is routinely achievable in experiments [80]. Aside from the spectral measurements neglecting angular information, it is likely this difference is due to the constant momentum resolution vs constant energy resolution, for which there is the following relationship $\Delta E = 1/2\Delta p^2 + p\Delta p$. Thus, for the region $p \in [0, 1]$ a.u., where the majority of signal is located, the fixed 0.1 a.u. momentum resolution varies from 0.005 – 0.105 a.u. resolution in energy. This gives a lower average resolution of this region but a higher resolution in the region where the distribution is maximum, and thus leads to a lower uncertainty than that of the spectral measurement. The resolution of detection setups used in strong field physics does not exhibit constant resolution as shown here but will vary quantifiably, often dependent on tuning the guiding electric and magnetic fields [80].

In Table I the square root of the ratio between the quantum and the classical Fisher informations for a single

	5	10	20	Mono
full	24.328822	54.805266	77.883953	89.462169
yield	24.742480	55.700743	79.153587	90.920518
coarse	24.336157	54.821454	77.906904	89.488510
spec	24.347465	54.860459	77.967933	89.560844
spec coarse	24.352390	54.870148	77.981217	89.575920

TABLE I. Increase in uncertainty of the classical vs quantum Fisher information for the full momentum, yield, coarse momentum, spectral and coarse spectral measurements, neglecting interference. Computed using $\sqrt{Q_F(t_f)/I_F(t_f)}$, where t_f is the time at the end of the pulse. This relates to using only a single channel for ionization. We choose the ionization event that occurs at the peak intensity of the laser. All parameters are the same as Fig. 3.

	5	10	20	Mono
full	3.727896	3.029688	2.322227	1.972497
yield	25.965643	30.805221	31.886580	31.337388
coarse	10.072111	12.156392	8.328323	7.011814
spec	4.685787	3.392254	2.346648	1.971997
spec coarse	20.580409	23.347627	15.053142	15.591103

TABLE II. Same as Table I except 5 intercycle channels of ionization are included. These are the first 5 ionization events that occur after the half maximum of each pulse, $-\tau/2$. Any relevant events after this are not considered in these results. All parameters are the same as Fig. 4.

ionization channel are displayed. This can be viewed as denoting how close the uncertainty derived from a specific classical Fisher information is compared to the best possible measurement, where a value of 1 would mean they are equal. Note, for Table I, the longer the pulse is the larger the ratio, this is because the quantum Fisher information will increase more rapidly for a longer pulse, while the classical Fisher information does not significantly increase when interference is neglected. The situation drastically changes when interference is included in Table II, the full classical Fisher information is much closer to the quantum case. With the uncertainty only 3.7 times minimum possible value for the 5 cycle pulse, reducing to 2.0 times this for the monochromatic case. The yield classical Fisher information stays at around 30 times the best

	5	10	20	Mono
full	2.627620	2.231962	1.993563	1.923594
yield	56.859871	32.893725	22.353922	31.975848
coarse	7.583439	9.502632	7.371176	6.649124
spec	4.431234	3.810768	2.234443	1.951190
spec coarse	20.225071	23.308732	16.617459	14.007984

TABLE III. Same as Table II except both pairs of ionization times are included for the all the 5 channels of ionization. All remaining parameters are the same as Fig. 3.

minimum possible uncertainty, thus is 7.5 – 15 less precise than the full classical Fisher information. The coarse classical Fisher information (with 0.1 a.u. resolution) is in-between at around 9 times the minimum uncertainty for a 5 cycle pulse. The complete spectral measurement is close to full momentum measurement, again due to the near spherical symmetry of the transition amplitude, which increases for longer pulses. The coarse spectral measurement for a resolution of 0.05 a.u. consistently leads to an uncertainty, twice that of the coarse momentum measurement. This is consistent with the factor of 5 observed between the classical Fisher informations.

In Table III both the ‘long’ and ‘short’ ionization times are included for all 5 channels of ionization. Hence, both intercycle and intracycle interference is included. This leads to further improvement in the full and coarse momentum measurement, as they get closer to the ideal quantum measurement, particularly for the 5 cycle pulse. The spectral measurement, however, remains at a similar value. This is due to the fact that there will be more angular dependence in the momentum distribution, which spectral measurement will not have access to. Thus, it is likely that more detailed intracycle interferences such as holographic interference patterns, which are not considered here, would lead to even larger differences between the full and spectral measurements.

This suggests that for a short 5 cycle pulse changing the measurement from a 0.05 a.u resolution spectral measurement to an arbitrarily high resolution full momentum measurement could reduce the laser uncertainty by 7.7 times. Considering the state of the art is around 1% [48, 51] uncertainty achieved for a spectral measurement with similar resolution, this could mean uncertainty lower than 0.13%. However, these experiments used different pulse length of 2-3 cycles in Ref. [48] and 15 cycles in Ref. [51]. In the former a better estimate can be found by using only 3 cycles (see Sec. IV B Table IV). The latter experiment has a pulse long enough and strong enough such that depletion of the bound state should be accounted for. This has not been considered in the current framework. Thus, we must keep the probability of remaining in the bound portion of the wavefunction near one and uncertainty derived from long or high intensity pulses should be treated with caution. This is discussed in more detail in Sec. IV A 3.

To further reduce the uncertainty one could change the experimental setup entirely to measure the ponderomotive phase (in line with the quantum Fisher information), which reduces the uncertainty by an extra factor of 2.6. Of course, simply doing more measurements will also reduce the uncertainty. However, a reduction by a factor of 10 requires 100 times more measurements. This quickly becomes difficult as various experimental parameters can not be controlled/ kept stable enough for extended periods of time, thus there is limit on the acquisition time. However, with increased repetition rates of lasers from 1 khz to over 100 khz, this kind of increase can already be achieved.

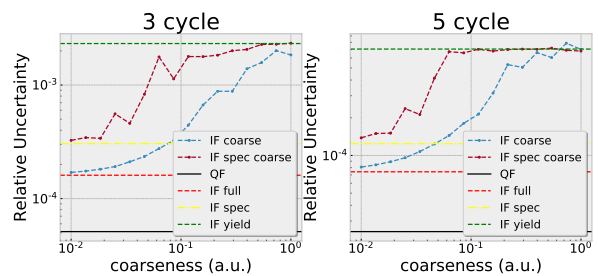


FIG. 5. The uncertainty in laser intensity for coarse measurements with different resolutions. On the left is a 3 cycle pulse, on the right is a 5 cycle pulse. The laser intensity is 2×10^{14} W/cm².

2. Coarseness

In Sec. III we presented the formulation for the full, coarse and yield measurements. The full and yield measurements are opposite limits of the coarse case, where full corresponds to infinite precision measurements ($\Delta p \rightarrow 0$ or $\Delta E \rightarrow 0$) and yield corresponds to no precision ($\Delta p \rightarrow \infty$ or $\Delta E \rightarrow \infty$). In Fig. 5 we examine the effect of reducing the coarseness from 1. a.u. to 0.01 a.u. (in momentum and energy resolution) on the relative uncertainty $\Delta U_p/U_p$, where ΔU_p is given by the Cramér-Rao bound (Eq. (16)). As expected from the above arguments, the relative uncertainty asymptotically tends to the value derived from the full classical Fisher information.

It is of note that, for the parameters chosen here, increasing the precision only reduces the laser intensity uncertainty [Fig. 5 (a)] up to a point. Increasing precision from 1 – 0.1 a.u. leads to an order of magnitude decrease in uncertainty but changing the precision from 0.1 – 0.01 a.u. leads only to a factor of two decrease in uncertainty. By 0.01 precision the value of IF coarse is nearly that of IF full so increasing the precision further will not appreciably reduce the laser intensity uncertainty. Thus, there are diminishing returns to increasing the momentum precision. It does mean that the uncertainty presented here, derived from full momentum measurements, should be realistically achievable in experiment as 0.01 a.u. resolution is not much beyond that achieved in existing setups [80].

3. Pulse Length and Laser Intensity Trends

In Fig. 6 the relative laser intensity uncertainty is plotted vs an increasing pulse length. All ionization channel intracycle and intercycle have been included for each pulse. Note that the relative uncertainty derived from full classical Fisher and quantum Fisher information both follow $n^{-3/2}$ scaling over the number of cycles n . This corresponds to a cubic scaling in the respective Fisher informations. This is due to a combination of quadratic

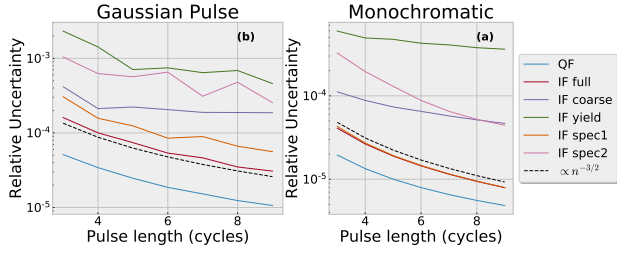


FIG. 6. The quantum and classical Fisher information with an increasing number of laser cycles. In the monochromatic case, the number of cycles corresponds to the number of ionization events included. The laser intensity is 2×10^{14} W/cm². The remaining field and target parameters are the same as Fig. 3.

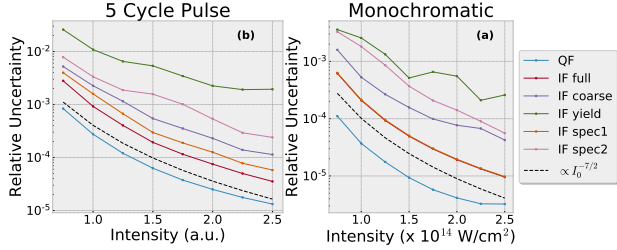


FIG. 7. Uncertainty with increasing laser intensity derived from the quantum and classical Fisher informations for a 5 cycle and monochromatic laser field. The remaining field and target parameters are the same as Fig. 3.

scaling with the pulse length due to interference combined with additional linear scaling as an increasing the pulse length linearly increases the signal/ portion of the electron that is ionized. It is clear from the previous analytic and numerical results that the quantum Fisher information quadratically increases with the time that the laser is on, while the full classical Fisher information follows the same trend due to interferences.

In Fig. 7 we look at the relative uncertainty in the laser intensity as the intensity itself varies. The main reason for considering laser intensity as a measurement variable is the high sensitivity of non-linear ionization processes on the laser intensity. Thus, it should be expected that there is a very strong dependence of the laser intensity uncertainty when varying the intensity. Indeed, we find in the region of interest the quantum Fisher information roughly follows a $I^{-7/2}$ power scaling. The $I^{-7/2}$ power scaling will not hold over all intensity ranges but it allows us to demonstrate the high sensitivity of the laser intensity uncertainty. Given we are altering the parameter that is being measured and computing relative uncertainty, the error is divided by U_p which will show up in this scaling.

Beyond a certain laser intensity and pulse length depletion of the target will start to play a role and the trend of reducing uncertainty will not persist in either case. This will act to limit the quantum and classical Fisher informations beyond a particular combination of

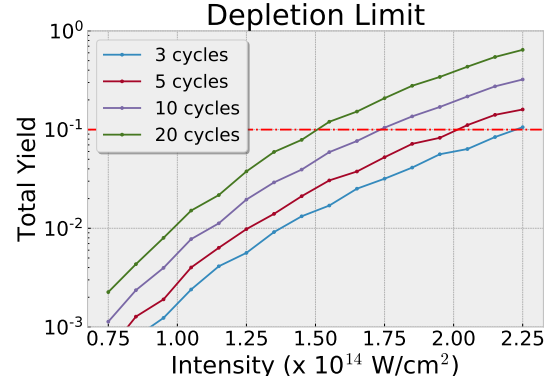


FIG. 8. Total ionization yield vs intensity for different length Gaussian pulses, in figure legend. This is computed by integrating the momentum probability distribution. A log scale has been used for the total yield. The red line marks 10% total ionization. For any laser parameters that lead to a yield above the Fisher information computations will start to break down. The remaining field and target parameters are the same as Fig. 3.

laser intensity and pulse length. Given our model does not account for depletion we must ensure the total ionized portion of the wavefunction stays well below 1. In Fig. 8 we show the total probability yield of the ionized portion of the wavefunction. A line at 10% ionization yield is plotted on the figure, if the yield is above this line then the Fisher information computations should be treated with care. In Fig. 8 the 3, 5, 10 and 20 cycle Gaussian pulses reach 10% ionization at 2.25×10^{14} , 2.0×10^{14} , 1.75×10^{14} and 1.5×10^{14} W/cm², respectively. This gives a limit on what can be realistically predicted with this model. Given these limitations it is possible to project the lowest possible uncertainty theoretically achievable, within the bounds of this model. For a 5-cycle pulse at 2.0×10^{14} W/cm² given 5×10^4 measurements the relative uncertainty derived from the quantum Fisher informations would be $2.8 \times 10^{-3}\%$, while for the full momentum measurement it is $7.4 \times 10^{-3}\%$. It should be noted that achieving this very low uncertainty may be difficult and these values should be taken with a pinch of salt. The computation of these uncertainty makes certain assumptions. For example, it is assumed that the theory is a very good match can be fitted to the experiment to obtain the uncertainty. However, there will be some mismatch and it is very difficult to account for how this will affect the final uncertainty.

B. Replicate previous work/ predictions

In this section we will compare the relative laser intensity uncertainty from our computations with that obtained in [48]. In [48] a TDSE generated spectrum was fitted to experimental results to compute the uncertainty for intensities in the range $1 \times 10^{14} - 5 \times 10^{14}$ W/cm²

$I(10^{14} \text{ W/cm}^2)$	Exp (%)	QF (%)	IF full (%)	IF 0.1 (%)	IF yield (%)	IF spec full (%)	IF spec coarse (%)
1.13	1.77	0.040	0.20	0.38	0.58	0.31	0.51
1.53	1.31	0.014	0.062	0.11	0.20	0.091	0.11
1.82	1.10	0.011	0.048	0.074	0.19	0.068	0.10

TABLE IV. The relative uncertainty experimentally determined in [48] and calculated using the quantum Fisher information (QF) and the full (IF full), coarse (IF 0.1, where the resolution is denoted in atomic units), yield (IF yield), full spectra (IF spec) and coarse spectra (IF spec coarse, the resolution is set by the experiment and varies between each intensity data set) classical Fisher information. The intensities are given in (10^{14} W/cm^2 units) and cover the lowest three values in the range covered by [48]. The number of measurements is set as 4.3×10^5 , 4.1×10^5 and 2.1×10^5 , from top to bottom, corresponding to the number of measurements in each data set.

for 2–3 cycle pulses. For each data point in the spectra 10^4 measurement were made, there are between 6 – 46 points in each spectra, the number of measurements in the Cramér-Rao bound Eq. (16) is set accordingly. The error quoted is 1% over the whole range of intensities. However, a closer look does reveal a slight trend of higher accuracy for higher intensity, as predicted in the previous section. In Table IV we compute the uncertainty using the quantum and classical Fisher information for intensities in the range quoted and a 3-cycle pulse length near the 6.3 fs given in the experiment.

In Table IV the uncertainties achieved in [48] are listed in the column *Exp (%)*. The final column *IF spec coarse* is constructed to mimic the experimental measurement procedure. For these values a coarse spectrum measurement was used for the classical Fisher information, where the measurement bin was set to the same size as used in each intensity data set. The values are in all cases below that of the experiment. This is expected because, as previously stated, care must be taken given we are idealizing the experimental set up and the ability to match to theory. In particular in the experiment it was necessary to account for the focal volume of the laser in this experiment to achieve these uncertainties [48]. This effect increases with the laser intensity [81], which is consistent with a less good match in the uncertainty for larger laser intensity.

From the results presented here it should be expected that the uncertainty would reduce for larger intensities, however it may be that focal averaging may be preventing this but as previously stated it is possible to design experiments to minimize this effect, which could lead to big reductions in the laser intensity uncertainty. Other effects such as background noise have also not been incorporated into the model, which will also act to increase the uncertainty.

The uncertainty from classical Fisher information measurements in Table IV follow the expected pattern, with the yield being the highest, followed by the coarse spectral (IF spec 0.05) and then the coarse momentum measurement (IF 0.1), full spectral and finally the full momentum measurement giving the most accuracy. It is apparent from Table IV that it is also possible to achieve considerable improvement in the uncertainty if another measurement basis is used. The quantum Fisher infor-

mation reducing to around one hundredth of a percent for the highest intensity. The large difference between QF and IF is likely due to the short pulse length, exhibiting less intercycle interference. Thus, another way to decrease the uncertainty in these measurements would be to use longer pulse lengths.

V. CONCLUSIONS

In this work we have developed a new framework for evaluating and understanding the uncertainty of *in situ* measurements in attoscience. The framework we have presented uses the tools and language of quantum sensing, common in quantum optics and quantum information and associated with high precision measurements [52–54, 82–85]. Recently, as attoscience has matured, both experiment and theory have become more precise and the conversation has turned from qualitative to quantitative measurements. Thus, it is timely and appropriate to consider a framework for understanding and controlling uncertainty in strong-field *in situ* measurements. This is particularly true for laser intensity uncertainty, where many improvements can be made and a unified procedure of determining laser intensity via *in situ* measurements would be very desirable.

Using this framework we explored many illuminating trends regarding the physical processes that govern the uncertainty in *in situ* measurements. Primarily, we demonstrated how interference of the photoelectron pathways can have a dramatic effect on the laser intensity uncertainty, as information about the latter builds up in the relative coherent phases of the electron state. In particular, these phases arise due to the coherent superposition between the bound and continuum states, which allow the continuum states acquire a phase difference we refer to as the ponderomotive phase. Interference is one of the most commonly exploited ways for determining quantum observables and it is no exception in strong field physics. It is already well-known that intercycle interference/ ATI-rings has strong laser intensity dependence [66]. Here, we make quantitative statements showing this interference vastly reduces the laser intensity uncertainty, by over 20 times in some examples. We also show subcycle or intracycle interference leads to further reductions

in the uncertainty.

Due to the great flexibility of this framework we are able to investigate many types of measurement, in particular we are able to account for uncertainty in the measurement apparatus in the form of coarse measurements. Thus, we can make direct statements about how the uncertainty in the measurement equipment affects the final laser intensity uncertainty. We found that beyond a certain cut-off additional precision will not strongly affect the uncertainty. This is a stepping stone from which it would be possible to use this framework to explicitly prototype detectors and optimize their efficacy for determining particular parameters. Comparisons of resolutions is a prime example of how this methodology can be used to evaluate different types of measurement/ detection for parameter estimation. By modelling the changing resolution present in detectors [80], experimental setups could be optimized for particular measurement. We foresee that this type of method could even be used in prototyping to guide the best detector designs given different measurement goals. In another optimization example, this framework could be used to determine whether a trade off between an increased control or precision in the measurement vs a reduction in counts is worth it in terms of how it affects the uncertainty of a measurement variable.

We also evaluated trends in the laser intensity uncertainty over increasing pulse length and laser intensity, and we find increasing sensitivity as both these parameters increase. Furthermore, direct comparison was made to *in situ* measurements made in [48], where the computation of the uncertainty was designed to follow the measurements made therein. Reduction in the uncertainty by 2-3 times may be possible by using high resolution 3D momentum measurements, while measuring in another non-momentum basis could give the capacity for a further 4-5 times reduction. Choosing a longer pulse length would yet further reduce the uncertainty.

It is important to note that due to effects like depletion, focal volume effects and CEP averaging, some care should be taken when comparing our theoretical predictions with experiment. We assume we have access to multiple copies of an identical wave function, when in fact, there are incoherent averaging effects such as variation of the intensity of over the focal volume and carrier envelope phase (CEP) averaging. Focal volume effects can be minimized in the experiment by reducing the size of the interaction region between the laser and gas jet [49]. Alternatively, one could shape the laser intensity spatial profile to exhibit a flat top (see [86, 87] for examples). To account for CEP averaging in experiment one

may stabilize the CEP for a single value (although this will reduce the counts and ultimately may not be worth doing). The effects of noise/ background counts was not accounted for in this first approach, which will reduce the computed uncertainties. The parameter dependence of signal-to-noise ratio could also affect the trends explored in this work.

Additionally, the use of the SFA leaves out effects such as Coulomb phases and distortions of the photoelectron, coupling with bound states and multi-electron interaction. The former maybe be addressed by using Coulomb-corrected approaches such as the CQSFA [25, 88–90] or directly employing numerical solutions of the time-dependent Schrödinger equation such as with the Qprop software [91]. However, computations of the Fisher information the integrals are numerically intensive even for the simple SFA model. Thus, faster quantum orbit models such as the CQSFA would be more appropriate and feasibility studies should be performed before attempting this with a numerical TDSE solver. Future work should focus on tackling the above-stated issues, in addition to implementing more detailed measurement procedures to better reflect experiment. This would enable quantitative modelling of uncertainty *in situ* measurement allowing for high levels of optimization.

Nonetheless, the framework for evaluating uncertainties presented here reveals the key physical processes involved for an ideal strong field system. The ponderomotive phase the photoelectron acquired in the continuum lead to the sensitive quadratic scaling with time. Beyond laser intensity, this opens the door for evaluating any parameters of interest in strong field ionization. Taking this one step further multiple field or target parameters could be measured, which is often desirable in attoscience. This theoretical means of calculating the uncertainty, will go side-by-side with the fitting procedures involved *in situ* measurements, allowing the derived uncertainties to be understood, giving the potential for them to be considerably improved.

VI. ACKNOWLEDGEMENTS

We would like to thank Marco Genoni for bring some of the latest literature to our attention. This work was in part funded by the UK Engineering and Physical Sciences Research Council (EPSRC). ASM acknowledges grant EP/P510270/1, which is within the remit of the InQuBATE Skills Hub for Quantum Systems Engineering. CFMF would like to acknowledge EPSRC grant EP/T019530/1. SB would like to acknowledge EPSRC Grants No. EP/N031105/1 and EP/S000267/1

[1] D. B. Milošević, G. G. Paulus, D. Bauer, and W. Becker, *Journal of Physics B: Atomic, Molecular and Optical*

- [2] W. Becker, F. Grasbon, R. Kopold, D. B. Milošević, G. G. Paulus, and H. Walther, *Advances in Atomic Molecular and Optical Physics* **48**, 35 (2002).
- [3] W. Becker, S. P. Goreslavski, D. B. Milošević, and G. G. Paulus, *Journal of Physics B: Atomic, Molecular and Optical Physics* **51**, 162002 (2018).
- [4] M. Lewenstein, P. Balcou, M. Y. Ivanov, A. L'Huillier, and P. B. Corkum, *Phys. Rev. A* **49**, 2117 (1994).
- [5] T. Shaaran and C. F. de Morisson Faria, *Journal of Modern Optics* **57**, 984 (2010), <https://doi.org/10.1080/09500340903414619>.
- [6] T. Shaaran, M. T. Nygren, and C. Figueira de Morisson Faria, *Phys. Rev. A* **81**, 063413 (2010).
- [7] C. Figueira de Morisson Faria and X. Liu, *Journal of Modern Optics* **58**, 1076 (2011).
- [8] P. B. Corkum, *Phys. Rev. Lett.* **71**, 1994 (1993).
- [9] W. Becker, *Quantum Semiclass. Opt.* **7**, 423 (1995).
- [10] M. Lein, *Journal of Physics B: Atomic, Molecular and Optical Physics* **40**, R135 (2007).
- [11] F. Krausz and M. Ivanov, *Rev. Mod. Phys.* **81**, 163 (2009).
- [12] P. Salières, A. Maquet, S. Haessler, J. Caillat, and R. Taïeb, *Reports on Progress in Physics* **75**, 062401 (2012).
- [13] H. Ni, N. Eicke, C. Ruiz, J. Cai, F. Oppermann, N. I. Shvetsov-Shilovski, and L.-W. Pi, *Phys. Rev. A* **98**, 013411 (2018).
- [14] C. Hofmann, A. S. Landsman, and U. Keller, *Journal of Modern Optics* **66**, 1052 (2019), <https://doi.org/10.1080/09500340.2019.1596325>.
- [15] U. S. Sainadh, H. Xu, X. Wang, A. Atia-Tul-Noor, W. C. Wallace, N. Douguet, A. Bray, I. Ivanov, K. Bartschat, A. Kheifets, R. T. Sang, and I. V. Litvinyuk, *Nature* **568**, 75 (2019).
- [16] O. Smirnova, Y. Mairesse, S. Patchkovskii, N. Dudovich, D. Villeneuve, P. Corkum, and M. Y. Ivanov, *Nature* **460**, 972 (2009).
- [17] Y. Mairesse, J. Higué, N. Dudovich, D. Shafir, B. Fabre, E. Mével, E. Constant, S. Patchkovskii, Z. Walters, M. Y. Ivanov, and O. Smirnova, *Phys. Rev. Lett.* **104**, 213601 (2010).
- [18] F. Calegari, D. Ayuso, A. Trabattoni, L. Belshaw, S. De Camillis, S. Anumula, F. Frassetto, L. Poletto, A. Palacios, P. Decleva, J. B. Greenwood, F. Martín, and M. Nisoli, *Science* **346**, 336 (2014).
- [19] F. Lépine, M. Y. Ivanov, and M. J. J. Vrakking, *Nature Photonics* **8**, 195 (2014).
- [20] A. I. Kuleff, N. V. Kryzhevoi, M. Pernpointner, and L. S. Cederbaum, *Phys. Rev. Lett.* **117**, 093002 (2016).
- [21] F. Calegari, A. Trabattoni, A. Palacios, D. Ayuso, M. C. Castrovilli, J. B. Greenwood, P. Decleva, F. Martín, and M. Nisoli, *Journal of Physics B: Atomic, Molecular and Optical Physics* **49**, 142001 (2016).
- [22] A. Schiffrin, T. Paasch-Colberg, N. Karpowicz, V. Apalkov, D. Gerster, S. Mühlbrandt, M. Korbman, J. Reichert, M. Schultze, S. Holzner, J. V. Barth, R. Kienberger, R. Ernstorfer, V. S. Yakovlev, M. I. Stockman, and F. Krausz, *Nature* **493**, 70 (2013).
- [23] M. Schultze, E. M. Bothschafter, A. Sommer, S. Holzner, W. Schweinberger, M. Fiess, M. Hofstetter, R. Kienberger, V. Apalkov, V. S. Yakovlev, M. I. Stockman, and F. Krausz, *Nature* **493**, 75 (2013).
- [24] Y. Huismans, A. Rouzée, A. Gijsbertsen, J. H. Jungmann, A. S. Smolkowska, P. S. W. M. Logman, F. Lépine, C. Cauchy, S. Zamith, T. Marchenko, J. M. Bakker, G. Berden, B. Redlich, A. F. G. Van Der Meer, H. G. Muller, W. Vermin, K. J. Schafer, M. Spanner, M. Y. Ivanov, O. Smirnova, D. Bauer, S. V. Popruzhenko, and M. J. J. Vrakking, *Science* **331**, 61 (2011).
- [25] C. F. de Morisson Faria and A. S. Maxwell, *Reports on Progress in Physics* **83**, 034401 (2020).
- [26] J. P. Marangos, *Journal of Physics B: Atomic, Molecular and Optical Physics* **49**, 132001 (2016).
- [27] S. V. Popruzhenko, *Journal of Physics B: Atomic, Molecular and Optical Physics* **47**, 204001 (2014).
- [28] C. F. de Morisson Faria, R. Kopold, W. Becker, and J. M. Rost, *Phys. Rev. A* **65**, 023404 (2002).
- [29] D. B. Milošević and W. Becker, *Phys. Rev. A* **66**, 063417 (2002).
- [30] J. Wassaf, V. Vénier, R. Taïeb, and A. Maquet, *Phys. Rev. A* **67**, 053405 (2003).
- [31] .
- [32] V. Strelkov, *Phys. Rev. Lett.* **104**, 123901 (2010).
- [33] M. Tudorovskaya and M. Lein, *Phys. Rev. A* **84**, 013430 (2011).
- [34] V. V. Strelkov, M. A. Khokhlova, and N. Y. Shubin, *Phys. Rev. A* **89**, 053833 (2014).
- [35] A. D. Shiner, B. E. Schmidt, C. Trallero-Herrero, H. J. Wörner, S. Patchkovskii, P. B. Corkum, J.-C. Kieffer, F. Légaré, and D. M. Villeneuve, *Nature Physics* **7**, 464 (2011).
- [36] Y.-J. Chen, S. Pabst, A. Karamatskou, and R. Santra, *Phys. Rev. A* **91**, 032503 (2015).
- [37] D. Faccialà, S. Pabst, B. D. Bruner, A. G. Ciriolo, S. De Silvestri, M. Devetta, M. Negro, H. Soifer, S. Stagira, N. Dudovich, and C. Vozzi, *Phys. Rev. Lett.* **117**, 093902 (2016).
- [38] Y.-J. Chen, S. Pabst, and R. Santra, *Journal of Physics Communications* **2**, 045024 (2018).
- [39] X. Hao, J. Chen, W. Li, B. Wang, X. Wang, and W. Becker, *Phys. Rev. Lett.* **112**, 073002 (2014).
- [40] A. S. Maxwell and C. F. d. M. Faria, *Phys. Rev. A* **92**, 023421 (2015).
- [41] A. S. Maxwell and C. F. d. M. Faria, *Phys. Rev. Lett.* **116**, 143001 (2016).
- [42] S. F. J. Laroche, A. Talebpour, and S. L. Chin, *Journal of Physics B: Atomic, Molecular and Optical Physics* **31**, 1215 (1998).
- [43] V. R. Bhardwaj, S. A. Aseyev, M. Mehendale, G. L. Yudin, D. M. Villeneuve, D. M. Rayner, M. Y. Ivanov, and P. B. Corkum, *Phys. Rev. Lett.* **86**, 3522 (2001).
- [44] I. V. Litvinyuk, K. F. Lee, P. W. Dooley, D. M. Rayner, D. M. Villeneuve, and P. B. Corkum, *Phys. Rev. Lett.* **90**, 233003 (2003).
- [45] P. B. Corkum, N. H. Burnett, and F. Brunel, *Phys. Rev. Lett.* **62**, 1259 (1989).
- [46] A. S. Alnaser, X. M. Tong, T. Osipov, S. Voss, C. M. Maharjan, B. Shan, Z. Chang, and C. L. Cocke, *Phys. Rev. A* **70**, 023413 (2004).
- [47] C. Smeenk, J. Z. Salvail, L. Arissian, P. B. Corkum, C. T. Hebeisen, and A. Staudte, *Opt. Express* **19**, 9336 (2011).
- [48] M. G. Pullen, W. C. Wallace, D. E. Laban, A. J. Palmer, G. F. Hanne, A. N. Grum-Grzhimailo, K. Bartschat, I. Ivanov, A. Kheifets, D. Wells, H. M. Quiney, X. M. Tong, I. V. Litvinyuk, R. T. Sang, and D. Kiehlinski, *Phys. Rev. A* **87**, 053411 (2013).
- [49] D. Kiehlinski, R. T. Sang, and I. V. Litvinyuk, *Journal of Physics B: Atomic, Molecular and Optical Physics* **47**,

- 204003 (2014).
- [50] C. Khurmi, W. C. Wallace, S. Sainadh U, I. A. Ivanov, A. S. Kheifets, X. M. Tong, I. V. Litvinyuk, R. T. Sang, and D. Kielpinski, *Phys. Rev. A* **96**, 013404 (2017).
- [51] C. Wang, X. Li, X.-R. Xiao, Y. Yang, S. Luo, X. Yu, X. Xu, L.-Y. Peng, Q. Gong, and D. Ding, *Phys. Rev. Lett.* **122**, 013203 (2019).
- [52] V. Giovannetti, S. Lloyd, and L. Maccone, *Nature Photonics* **5**, 222 (2011).
- [53] C. L. Degen, F. Reinhard, and P. Cappellaro, *Rev. Mod. Phys.* **89**, 035002 (2017).
- [54] K. Bongs, M. Holynski, J. Vovrosh, P. Bouyer, G. Condon, E. Rasel, C. Schubert, W. P. Schleich, and A. Roura, *Nature Reviews Physics* **1**, 731 (2019).
- [55] C. Helstrom, *Quantum detection and estimation theory* (Academic Press, New York, 1976).
- [56] M. G. A. Paris, *International Journal of Quantum Information* **07**, 125 (2009), <https://doi.org/10.1142/S0219749909004839>.
- [57] T. A. Wheatley, D. W. Berry, H. Yonezawa, D. Nakane, H. Arao, D. T. Pope, T. C. Ralph, H. M. Wiseman, A. Furusawa, and E. H. Huntington, *Phys. Rev. Lett.* **104**, 093601 (2010).
- [58] H. Yonezawa, D. Nakane, T. A. Wheatley, K. Iwasawa, S. Takeda, H. Arao, K. Ohki, K. Tsumura, D. W. Berry, T. C. Ralph, H. M. Wiseman, E. H. Huntington, and A. Furusawa, **337**, 1514 (2012).
- [59] Z. S. Tang, K. Durak, and A. Ling, *Opt. Express* **24**, 22004 (2016).
- [60] M. Paúr, B. Stoklasa, Z. Hradil, L. L. Sánchez-Soto, and J. Rehacek, *Optica* **3**, 1144 (2016).
- [61] F. Yang, A. Tashchilina, E. S. Moiseev, C. Simon, and A. I. Lvovsky, *Optica* **3**, 1148 (2016).
- [62] W.-K. Tham, H. Ferretti, and A. M. Steinberg, *Phys. Rev. Lett.* **118**, 070801 (2017).
- [63] J. M. Donohue, V. Ansari, J. Řeháček, Z. Hradil, B. Stoklasa, M. Paúr, L. L. Sánchez-Soto, and C. Silberhorn, *Phys. Rev. Lett.* **121**, 090501 (2018).
- [64] M. Parniak, S. Borówka, K. Boroszko, W. Wasilewski, K. Banaszek, and R. Demkowicz-Dobrzański, *Phys. Rev. Lett.* **121**, 250503 (2018).
- [65] M. B. Gaarde, J. L. Tate, and K. J. Schafer, *Journal of Physics B: Atomic, Molecular and Optical Physics* **41**, 132001 (2008).
- [66] M. Lewenstein, K. C. Kulander, K. J. Schafer, and P. H. Bucksbaum, *Phys. Rev. A* **51**, 1495 (1995).
- [67] B. B. Augstein and C. F. De Morisson Faria, *Modern Physics Letters B* **26**, 1130002 (2012).
- [68] S. Haessler, J. Caillat, W. Boutu, C. Giovanetti-Teixeira, T. Ruchon, T. Auguste, Z. Diveki, P. Breger, A. Maquet, B. Carré, R. Taïeb, and P. Salières, *Nature Physics* **6**, 200206 (2010).
- [69] J. Itatani, F. Quéré, G. L. Yudin, M. Y. Ivanov, F. Krausz, and P. B. Corkum, *Phys. Rev. Lett.* **88**, 173903 (2002).
- [70] E. Cormier, I. A. Walmsley, E. M. Kosik, A. S. Wyatt, L. Corner, and L. F. DiMauro, *Phys. Rev. Lett.* **94**, 033905 (2005).
- [71] J. Gagnon, E. Goulielmakis, and V. S. Yakovlev, *Applied Physics B* **92**, 25 (2008).
- [72] I. Orfanos, I. Makos, I. Lontos, E. Skantzakis, B. Frg, D. Charalambidis, and P. Tzallas, *APL Photonics* **4**, 080901 (2019), <https://doi.org/10.1063/1.5086773>.
- [73] D. D. Hickstein, P. Ranitovic, S. Witte, X.-M. Tong, Y. Huismans, P. Arpin, X. Zhou, K. E. Keister, C. W. Hogle, B. Zhang, C. Ding, P. Johnsson, N. Toshima, M. J. J. Vrakking, M. M. Murnane, and H. C. Kapteyn, *Phys. Rev. Lett.* **109**, 073004 (2012).
- [74] K. Amini, J. Biegert, F. Calegari, A. Chacón, M. F. Ciappina, A. Dauphin, D. K. Efimov, C. F. de Morisson Faria, K. Giergiel, P. Gniewek, A. S. Landsman, M. Lesiuk, M. Mandrysz, A. S. Maxwell, R. Moszyński, L. Ortmann, J. A. Pérez-Hernández, A. Picón, E. Pisanty, J. Prauzner-Bechcicki, K. Sacha, N. Suárez, A. Zar, J. Zakrzewski, and M. Lewenstein, *Reports on Progress in Physics* **82**, 116001 (2019).
- [75] W. Becker, S. Long, and J. K. McIver, *Phys. Rev. A* **50**, 1540 (1994).
- [76] D. Volkov, *Zeit. für Physik* **40**, 117 (1926).
- [77] D. Volkov, *Zeit. für Physik* **94**, 250 (1935).
- [78] W. Becker, A. Lohr, M. Kleber, and M. Lewenstein, *Phys. Rev. A* **56**, 645 (1997).
- [79] P. A. Korneev, S. V. Popruzhenko, S. P. Goreslavski, W. Becker, G. G. Paulus, B. Fetić, and D. B. Milošević, *New Journal of Physics* **14**, 055019 (2012).
- [80] B. Wolter, M. G. Pullen, M. Baudisch, M. Sclafani, M. Hemmer, A. Senftleben, C. D. Schröter, J. Ullrich, R. Moshhammer, and J. Biegert, *Phys. Rev. X* **5**, 021034 (2015).
- [81] R. Kopold, W. Becker, M. Kleber, and G. G. Paulus, *J. Phys. B* **35**, 217 (2002).
- [82] R. Demkowicz-Dobrzanski, M. Jarzyna, and J. Koodyski, *Chapter Four - Quantum Limits in Optical Interferometry*, edited by E. Wolf, *Progress in Optics*, Vol. 60 (Elsevier, 2015) pp. 345 – 435.
- [83] D. Braun, G. Adesso, F. Benatti, R. Floreanini, U. Marzolino, M. W. Mitchell, and S. Pirandola, *Rev. Mod. Phys.* **90**, 035006 (2018).
- [84] L. Pezzè, A. Smerzi, M. K. Oberthaler, R. Schmied, and P. Treutlein, *Rev. Mod. Phys.* **90**, 035005 (2018).
- [85] S. Pirandola, B. R. Bardhan, T. Gehring, C. Weedbrook, and S. Lloyd, *Nature Photonics* **12**, 724 (2018).
- [86] W. Boutu, T. Auguste, O. Boyko, I. Sola, P. Balcou, L. Binazon, O. Gobert, H. Merdji, C. Valentin, E. Constant, E. Mével, and B. Carré, *Phys. Rev. A* **84**, 063406 (2011).
- [87] E. S. Toma, P. Antoine, A. de Bohan, and H. G. Muller, *Journal of Physics B: Atomic, Molecular and Optical Physics* **32**, 5843 (1999).
- [88] A. S. Maxwell, A. Al-Jawahiry, T. Das, and C. Figueira de Morisson Faria, *Phys. Rev. A* **96**, 023420 (2017), [arXiv:1705.01518](https://arxiv.org/abs/1705.01518).
- [89] A. S. Maxwell, A. Al-Jawahiry, X. Y. Lai, and C. Figueira de Morisson Faria, *J. Phys. B: At. Mol. Opt. Phys.* **51**, 044004 (2018).
- [90] A. S. Maxwell and C. Figueira de Morisson Faria, *J. Phys. B: At. Mol. Phys.* **51**, 124001 (2018), [arXiv:1802.00789](https://arxiv.org/abs/1802.00789).
- [91] D. Bauer and P. Koval, *Comput. Phys. Commun.* **174**, 396 (2006), [arXiv:0507089](https://arxiv.org/abs/0507089) [physics].